Nano Research

ISSN 1998-0124 CN 11-5974/O4
https://doi.org/10.26599/NR.2026.94909212

Communication

Tandem organic–perovskite heterostructures toward red/green/blue distributed feedback lasers

Qi Zhang[1,2], Zhiyuan Zhang[2,3], Xuanxuan Wei[2], Zihan Xiao[2], Junbiao Peng[3](✉), Ruidong Xia[2](✉)

[1] School of Electronic and Optical Engineering, School of Flexible Electronics (Future Technology), Nanjing University of Posts and Telecommunications, Nanjing 210023, China

[2] Key Laboratory for Organic Electronics & Information Displays (KLOEID), Jiangsu-Singapore Joint Research Center for Organic/Bio Electronics & Information Displays, Institute of Advanced Materials (IAM), Nanjing University of Posts and Telecommunications, 9 Wenyuan Road, Nanjing 210046, China

[3] National Key Laboratory of Luminescence Materials and Devices, South China University of Technology, Guangzhou 510641, China

Nano Res., **Just Accepted Manuscript** • https://doi.org/10.26599/NR.2026.94909212
https://www.sciopen.com/journal/1998-0124 on Sep. 23, 2026

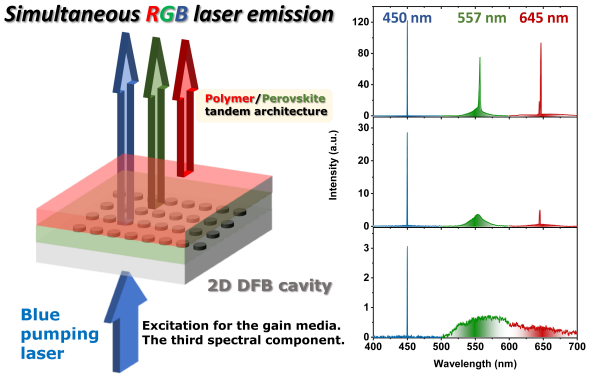
© The Authors(s)

Just Accepted

This is a "Just Accepted" manuscript, which has been examined by the peer-review process and has been accepted for publication. A "Just Accepted" manuscript is published online shortly after its acceptance,which is prior to technical editing and formatting and author proofing. Tsinghua University Press (TUP) provides "Just Accepted" as an optional and free service which allows authors to make their results available to the research community as soon as possible after acceptance. After a manuscript has been technically edited and formatted, and the page proofs have been corrected, it will be removed from the "Just Accepted" web site and published officially with volume and article number (e.g., *Nano Research*, **2025**, *18*, 94906990). Please note that technical editing may introduce minor changes to the manuscript text and/or graphics which may affect the content, and all legal disclaimers that apply to the journal pertain. In no event shall TUP be held responsible for errors or consequences arising from the use of any information contained in these "Just Accepted" manuscripts. To cite this anuscript please use its Digital Object Identifier (DOI®),which is identical for all formats of publication.

Just Accepted

TABLE OF CONTENTS (TOC)



An organic/perovskite tandem DFB device enables simultaneous RGB lasing by integrating the green and red emissions with the transmitted blue excitation laser.

Just Accepted

Nano Research

Open Access

Research Article

Tandem organic–perovskite heterostructures toward red/green/blue distributed feedback lasers

Qi Zhang[1,2], Zhiyuan Zhang[2,3], Xuanxuan Wei[2], Zihan Xiao[2], Junbiao Peng[3] and Ruidong Xia[2]

1 School of Electronic and Optical Engineering, School of Flexible Electronics (Future Technology), Nanjing University of Posts and Telecommunications, Nanjing 210023, China
2 Key Laboratory for Organic Electronics & Information Displays (KLOEID), Jiangsu-Singapore Joint Research Center for Organic/Bio Electronics & Information Displays, Institute of Advanced Materials (IAM), Nanjing University of Posts and Telecommunications, 9 Wenyuan Road, Nanjing 210046, China
3 National Key Laboratory of Luminescence Materials and Devices, South China University of Technology, Guangzhou 510641, China

Received: 8 July 2026; **Revised:** 29 August 2026; **Accepted:** 23 September 2026

Address correspondence to Ruidong Xia, iamrdxia@njupt.edu.cn; Junbiao Peng, psjbpeng@scut.edu.cn

Cite this article: *Nano Research*, 2026, 19, 94909212 https://doi.org/10.26599/NR.2026.94909212

ABSTRACT: Achieving multi-wavelength lasing in a single nanoscale device poses significant challenges, due to the stringent requirements for gain medium and microcavity design. Here, we present a tandem device using methylammonium lead bromide ($MAPbBr_3$) and a blend of poly(9,9-dioctylfluorene-alt-benzothiadiazole) (F8BT) with poly(3-hexylthiophene-2,5-diyl) (P3HT) as the gain media, both of which are deposited via a simple spin-coating process. The immiscibility between the polymer blend and the perovskite enables direct sequential deposition without an intermediate layer, yielding excellent interfacial quality. Electromagnetic simulations agree well with experiments and confirm that a 130 nm polymer blend and a 70 nm perovskite layer sustain distinct waveguiding modes. This gives rise to dual-wavelength amplified spontaneous emission (ASE) at 655 nm (F8BT:P3HT blend) and 548 nm ($MAPbBr_3$) with moderate thresholds. Furthermore, by using second-order, two-dimensional distributed feedback (DFB) gratings as the cavity, simultaneous red (645 nm) and green (557 nm) lasing was obtained at excitation pulse energies exceeding 480 $\mu J \cdot cm^{-2}$. In conjunction with the transmitted blue excitation laser (450 nm), red-green-blue (RGB) lasing was attained from the same single DFB device. The concept of the ultracompact RGB nanolaser paves the way toward future laser display technologies.

KEYWORDS: organic-perovskite hybrid laser; multicolor laser; 2D DFB cavity; multilayer device

1 Introduction

Cost-effective, multi-wavelength coherent semiconductor laser sources are in high demand for applications such as white-light generation, micro-optoelectronics, high resolution displays and biological sensing. Compared with conventional illumination sources, e.g., light emitting diodes, lasers offer potentially higher output power, better spectral resolution and superior directionality. In recent decades, considerable efforts have been devoted to developing multicolor micro/nano lasers with diverse gain media through various strategies [1-6]. Of the various candidates, organic and perovskite materials are promising gain media for fabricating highly-efficient multicolor micro/nano lasers, attributable to their outstanding optoelectronic characteristics, such as broad emission spectra, high color purity, and high photoluminescence quantum yields (PLQY). In recent years, significant progress has been made in both organic [7-9] and perovskite [10-13] devices in the pursuit of electrically pumped lasers. These approaches lay the groundwork for the practical application of organic and perovskite lasers [14]. On the other hand, vertically stacking multiple units is a common strategy to realize opto-electronic devices with broader or switchable operating band and higher performance, as seen in both light emitting diodes (LEDs) and solar cells [15-17]. A recent report describes a tandem perovskite LED featuring a photon recycling regime, which exhibits a notable 45.5% external quantum efficiency (EQE), owing to enhanced light outcoupling from trapped modes [15]. Organic and perovskite materials are attractive partners for multijunction architectures, as they share similar processing technologies while offering complementary properties. Organic/perovskite tandem devices can exploit the merits of both materials while compensating for their respective limitations [18-21]. With a rationally designed device architecture and well-tailored photoluminescence (PL) spectral overlap, hybrid organic/perovskite tandem LEDs can deliver both a large color gamut and excellent color purity simultaneously [20]. This is because the organic unit exhibits broad emission band, while the perovskite unit features narrow emission band, enabling complementary spectral coverage, making their hybrid tandem architecture a promising route for developing high-performance semiconductor luminescent devices.

In our previous work, we have demonstrated fully-polymeric multi-wavelength laser devices fabricated via a simple spin coating method [26]. Compared with previously reported approaches [22-24], the direct deposition of two orthogonally soluble polymers onto a distributed-feedback (DFB)-grating-patterned quartz substrate offers simpler processing without

Just Accepted

requiring complex fabrication technologies and specialized materials. However, one of the key challenges of this approach lies in identifying a water- or alcohol- soluble organic gain medium to serve as the bottom layer. Since most organic compounds are poorly soluble in water or alcohol. Other critical aspects, such as re-absorption among different mediums, resonator design for local electromagnetic field enhancement at varying wavelengths and interface engineering between thin-film layers, must also be addressed when constructing tandem laser devices.

Herein, we present our recent work on multicolor DFB lasers based on a tandem structure that integrates polymeric and perovskite gain media. To enable simultaneous excitation using a single blue laser source (450 nm), we employed methylammonium lead bromide ($MAPbBr_3$) as the bottom layer and deposited a red-emitting blend of poly(9,9-dioctylfluorene-alt-benzothiadiazole) (F8BT) and poly(3-hexylthiophene-2,5-diyl) (P3HT) on top. The perovskite thin-film showed great tolerance against the organic solvent providing a high-quality interface beneath the organic layer. The immiscibility of the perovskite and the polymer blend enabled the use of simple solution processing methods, such as spin coating, without needing an intermediate layer. The spectral separation between the organic and perovskite emission bands, combined with good confinement in their respective high refractive index regions, resulted in thinned active layers (130 nm for the polymer blend and 70 nm for the perovskite layer) and reduced re-absorption within the device. In the tandem device (130 nm F8BT:P3HT/70 nm $MAPbBr_3$/Quartz), the amplified simultaneous emission (ASE) band of each active layer exhibited a negligible shift (~1 nm) relative to its single-layer counterpart, demonstrating effective light confinement. Using a substrate pre-patterned with DFB gratings featuring periods of 330 nm and 390 nm, simultaneous lasing from both the perovskite (at 557 nm) and the polymer (at 645 nm) was obtained in the tandem device at a pump fluence of 480 $\mu J \cdot cm^{-2}$ exceeding the thresholds of both layers. As the blue excitation laser (450 nm) partially transmitted through the device, it combined with the emissions from the perovskite and polymer layers, yielding red-green-blue (RGB) laser output. This approach, wherein the feedback structure is predefined on the substrate prior to film deposition, circumvents the need for micro-structure engineering during thin-film processing. Consequently, it is well-suited for scalable, large-area solution processing techniques, including inkjet printing, slot-die coating and roll-to-roll manufacturing.

2 Results and Discussion

Early investigations demonstrated that lead acetate ($Pb(OAc)_2$), when employed as the lead source, yielded perovskite films with improved uniformity and reproducibility [25]. This fabrication method offers a streamlined process, as it requires no additives, anti-solvent treatment, or extended post-casting annealing. Therefore, in this study, the same "one-step" method was employed in preparation of $MAPbBr_3$ films. A series of precursor solutions with various concentrations of $Pb(OAc)_2$ (0.2, 0.4, 0.5, 0.6, 0.8, 1.0 mmol/mL (M)) were prepared in N,N-Dimethylformamide (DMF). $MAPbBr_3$ films with varying thicknesses were prepared by spin-coating the different precursor solutions described above (denoted as 0.2-1.0 M in Fig. 1(a)) under identical conditions. Detailed procedures are given in the "Experimental" section. All perovskite films exhibited the expected crystalline phase of $MAPbBr_3$, as confirmed by X-ray diffraction (XRD) measurements (Fig. S1 in the Electronic Supplementary Material (ESM)). In the XRD patterns of all films, distinct diffraction peaks are observed at 14.82°, 30.02° and 45.75° which are assignable to the (100), (200) and (300) crystal planes of the perovskite cubic phase, confirming the formation of $MAPbBr_3$. The thicknesses of the resulting $MAPbBr_3$ films ranged from ~19 to 192 nm as shown in Fig. 1(a). This is critical for the further application of perovskite films in the tandem thin-film laser devices, since the thickness must be modified to satisfy the multimode waveguiding conditions required for achieving simultaneous emission from different active layers.

The ASE performance of the perovskite films with different thickness was measured under identical

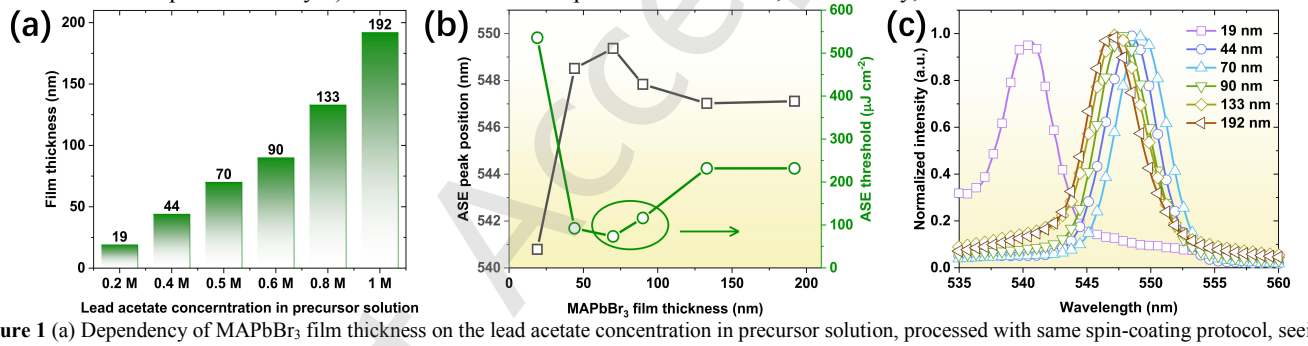


Figure 1 (a) Dependency of $MAPbBr_3$ film thickness on the lead acetate concentration in precursor solution, processed with same spin-coating protocol, seeing details in the "Experimental" section. (b) ASE peak positions (black open squares), thresholds (green open circles) and (c) typical ASE spectra well above threshold for $MAPbBr_3$ film with different thicknesses.

Just Accepted

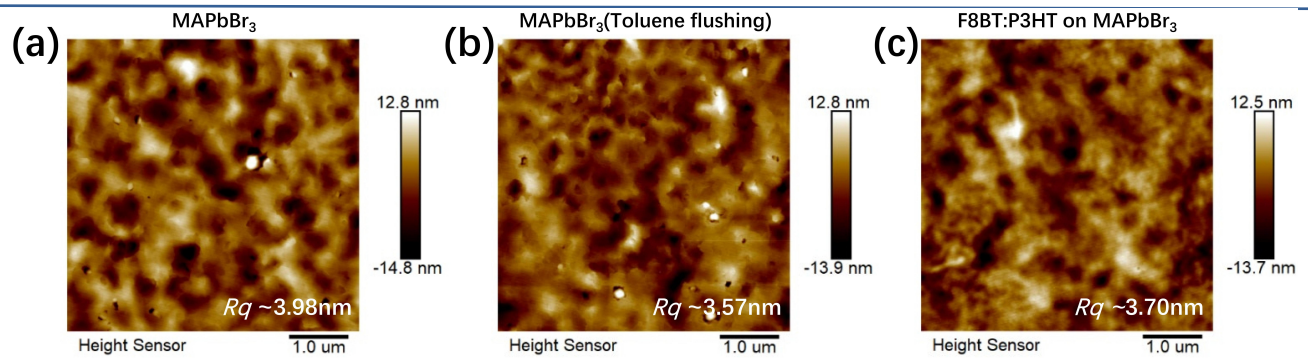


Figure 2 Atomic force microscopic images of $MAPbBr_3$ film: (a) without toluene flushing (b) with toluene flushing and (c) F8BT:P3HT on $MAPbBr_3$.*Rq* is the root mean square (RMS) roughness.

conditions using a 450 nm nanosecond laser as the excitation source (seeing details in the "Experimental" section). The ASE peak positions and thresholds measured for perovskite films with varying thicknesses are shown in Fig. 1(b), while the corresponding ASE spectra are presented in Fig. 1(c). Except for the ultra-thin $MAPbBr_3$ film (~19 nm thick), the ASE spectra of all perovskite films with different thickness peak between 547 and 549 nm, corresponding to a similar waveguiding mode across these samples. The ASE peak of the ultra-thin perovskite film is at 541 nm. This blue shift of the ASE peak relative to those of other thicker samples and reference data, suggests insufficient light confinement and higher optical loss in such thin film. This trend is further reflected in the ASE threshold values. While thicker $MAPbBr_3$ films exhibited relatively similar thresholds in the range of 92-231 $\mu J \cdot cm^{-2}$, the ultra-thin perovskite film required a significantly higher excitation fluence of 550 $\mu J \cdot cm^{-2}$. Overall, the ASE characterization results demonstrate that $MAPbBr_3$ films maintain good optical gain over a wide thickness range. This provides considerable flexibility for the tandem laser device integration discussed below.

As established in our prior work [26], a smooth and uniform interface between different active layers is critical for achieving efficient multi-wavelength output in multilayer devices. The red-emissive F8BT:P3HT polymer blend was employed as the upper layer medium in the device. The F8BT:P3HT blend offers a low ASE threshold, high PL efficiency, and a relatively high refractive index [27-29]. Given that the polymer blend is readily soluble in toluene

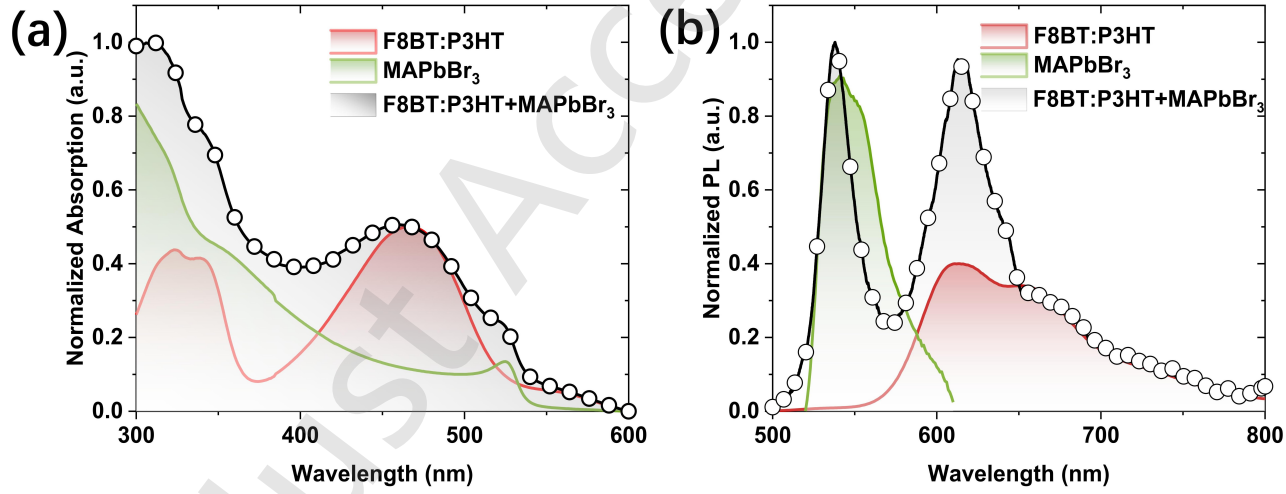


Figure 3 (a) Absorption and (b) photoluminescence spectra of the tandem device (black line and open circles), along with those of the F8BT:P3HT blend (red line) and the $MAPbBr_3$ (green line) single-layer devices.

(an orthogonal solvent for perovskite), the effect of toluene exposure on the underlying perovskite film was assessed using atomic force microscopy (AFM). 100 µL of toluene was spin coated onto the perovskite surface. The AFM images of the perovskite films with and without toluene exposure are compared in Figs. 2(a) and 2(b), showing no significant change. The root-mean-square (RMS) roughness values for the two cases are comparable (3.57 nm and 3.98 nm, respectively), demonstrating that the perovskite film is highly tolerant to toluene. Therefore, the deposition of the polymer layer from a toluene solution introduces negligible damage to the underlying perovskite layer. The morphology of the F8BT:P3HT blend layer (~130 nm thick) deposited on the perovskite was also characterized, as shown in Fig. 2(c). The surface of the polymer layer is flat and homogeneous (RMS roughness~3.7 nm). Given the high quality of the perovskite/polymer interface and the top surface of the polymeric layer, a well-defined double-layer waveguide is established. The absorption and PL spectra of the tandem device are shown in Figs. 3(a) and 3(b), respectively, along with those of single-layer devices. The tandem device exhibits a broad absorption spectrum resulting from the superposition of the absorption spectra of its constituent polymer and perovskite layers. The characteristic peaks of F8BT:P3HT blend (326 nm, 341 nm and 465 nm) and $MAPbBr_3$ (353 nm and 525 nm) are all evident in the absorption spectrum of the tandem device. In the PL spectrum, the tandem device shows two main peaks at 550 nm and 630 nm which can be assigned to the emission from $MAPbBr_3$ and F8BT:P3HT blend, respectively. However, the shape of PL peaks in the tandem device is narrower compared with that in the single-layer device. The

Just Accepted

strong enhancement observed at 620 nm, which can be assigned to the 0–0 emission peak of F8BT:P3HT, is attributed to the formation of interchain complexes between the two polymers upon deposition onto the perovskite film [30-31].

To define the tandem device structure, the thickness of each the ESM), a simulation model was constructed. The model consists of a quartz substrate layer, an active layer (with active layer of the tandem device divided into two sub-layers), and an air cladding layer. For the $MAPbBr_3$ single-layer device, active layer must be determined. Electromagnetic simulations were performed to guarantee the establishment and propagation of proper optical modes in the devices. By combining the PL and refractive index spectra (see Fig. S2 in

simulations indicate that the characteristic emission at 548 nm can be sustained in the model at an active layer thickness of 70 nm (Fig. 4(a)). The

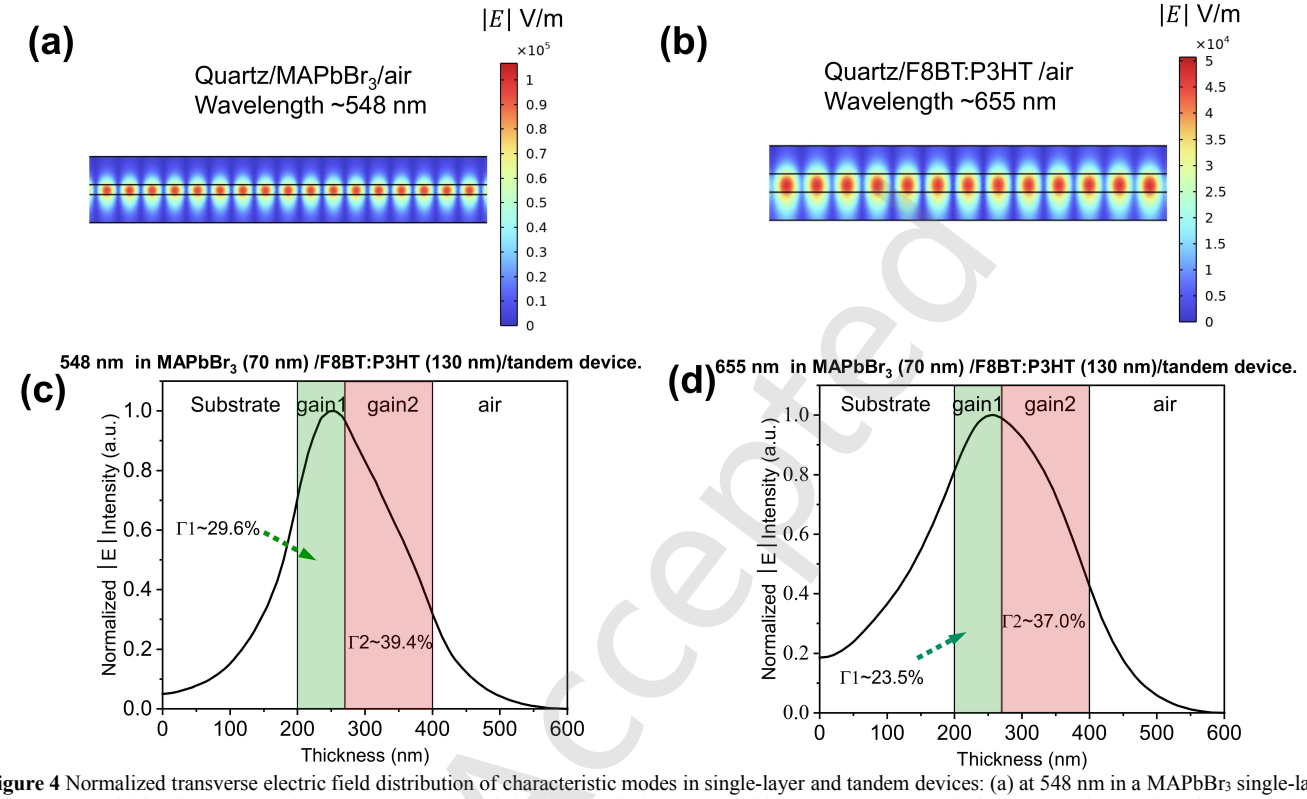


Figure 4 Normalized transverse electric field distribution of characteristic modes in single-layer and tandem devices: (a) at 548 nm in a $MAPbBr_3$ single-layer device (70 nm thick); (b) at 655 nm in an F8BT:P3HT blend single-layer device (130 nm thick); (c) at 548 nm and (d) at 655 nm in a tandem device consisting of F8BT:P3HT (130 nm) and $MAPbBr_3$ (70 nm). Γ1 and Γ2 denote the confinement factors at 548 nm and 655 nm in the perovskite (gain 1) and polymer (gain 2) layers, respectively.

excellent agreement between this result and the experimental measurements reported above, validates the model as both robust and effective for our intended application. Similarly, for the F8BT:P3HT blend single-layer device, the characteristic emission at 655 nm is supported at an active layer thickness of 130 nm (Fig. 4(b)). The simulation results yield confinement factor Γ of 35.7% and 44.3% in the gain region at 548 nm and 655 nm, respectively, for single-layer devices (Figs. S3(a) and S3(b) in the ESM). For the tandem device, the simulation was designed to simultaneously support two characteristic emission peaks (548 nm and 655 nm) within their respective active layers. Figures 4(c) and 4(d) plot the normalized transverse electric field profiles of the corresponding characteristic modes at 548 nm and 655 nm, respectively, Under the optimized thickness conditions (130 nm polymer/70 nm perovskite). The confinement factor at 548 nm in the 70 nm perovskite layer is 29.6%, while that at 655 nm in the 130 nm polymer layer is 37.0%. Compared with single-layer device, the tandem device exhibits only a slight decrease (<7%) in confinement factor at the characteristic resonance wavelength within its gain layers. The characteristic optical modes at 548 nm and 655 nm are well-localized within their corresponding active layers. Figures S3(c) and S3(d) in the ESM, show the normalized transverse electric field profiles of the same characteristic modes under non-optimized conditions, revealing poor confinement. Based on the simulation, the perovskite and polymer layer thicknesses in the tandem device were optimized to 70 nm and 130 nm, respectively.

In order to evaluate the optical gain properties of the tandem device, ASE tests were carried out using a 450 nm nanosecond pulse laser as the pumping source. The F8BT:P3HT blend and the $MAPbBr_3$ films were excited sequentially by the laser incident from the polymer side. Consistent with our prior report [26], dual-band ASE emerged once the pump power exceeded the respective thresholds of the both gain media. Figure 5(a)

Just Accepted

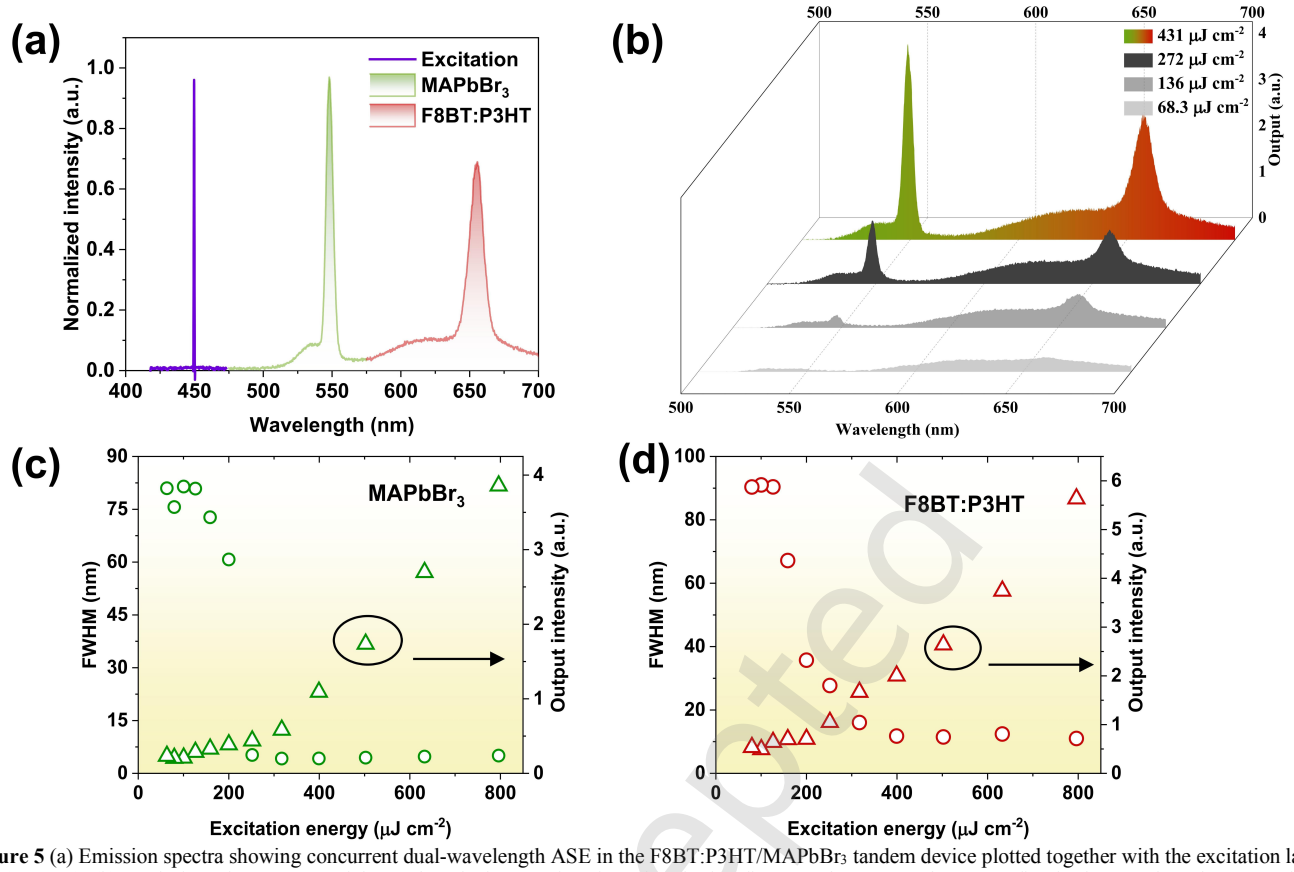


Figure 5 (a) Emission spectra showing concurrent dual-wavelength ASE in the F8BT:P3HT/$MAPbBr_3$ tandem device plotted together with the excitation laser line (450 nm). (b) Evolution of PL spectra of the tandem device as a function of excitation fluence. The ASE peak appears first in the $MAPbBr_3$ layer, resulting from a lower threshold. FWHM and output intensity of the $MAPbBr_3$ (c) and F8BT:P3HT (d)layers in the tandem device are plotted as a function of excitation energy.

displays the dual-peak ASE spectra measured from the tandem device, with the pump laser also shown, while Fig. 5(b) presents the evolution of the emission spectra as a function of increasing excitation fluence. The ASE peaks appear at 548 nm (FWHM~4.3 nm) and 655 nm (FWHM~11 nm), corresponding to the emission of $MAPbBr_3$ and F8BT:P3HT blend. In the tandem device, the ASE thresholds of $MAPbBr_3$ and F8BT:P3HT are 251 μJ·cm^{-2} and 316 μJ·cm^{-2}, respectively, as shown in Figs. 5(c) and 5(d). The ASE performance of the $MAPbBr_3$ and F8BT:P3HT blend single-layer device is shown in Fig. S4 in the ESM. All the ASE related results are summarized in Table 1. Compared with their single-layer counterparts, the active media in the tandem device shows substantially increased ASE thresholds, while their emission peak positions and FWHM remain similar. In $MAPbBr_3$, the ASE threshold increases from 73 μJ·cm^{-2} to 251 μJ·cm^{-2}, while in the upper layer, the ASE threshold of F8BT:P3HT increases even more significantly, from 6.8 μJ·cm^{-2} to 316 μJ·cm^{-2}. The elevated ASE thresholds in the tandem device, relative to its single-layer counterparts, partially corroborate the reduced optical confinement predicted by the simulations. More complex factors, such as re-absorption, interface defects, and the deterioration of optical waveguiding conditions may also play a

Just Accepted

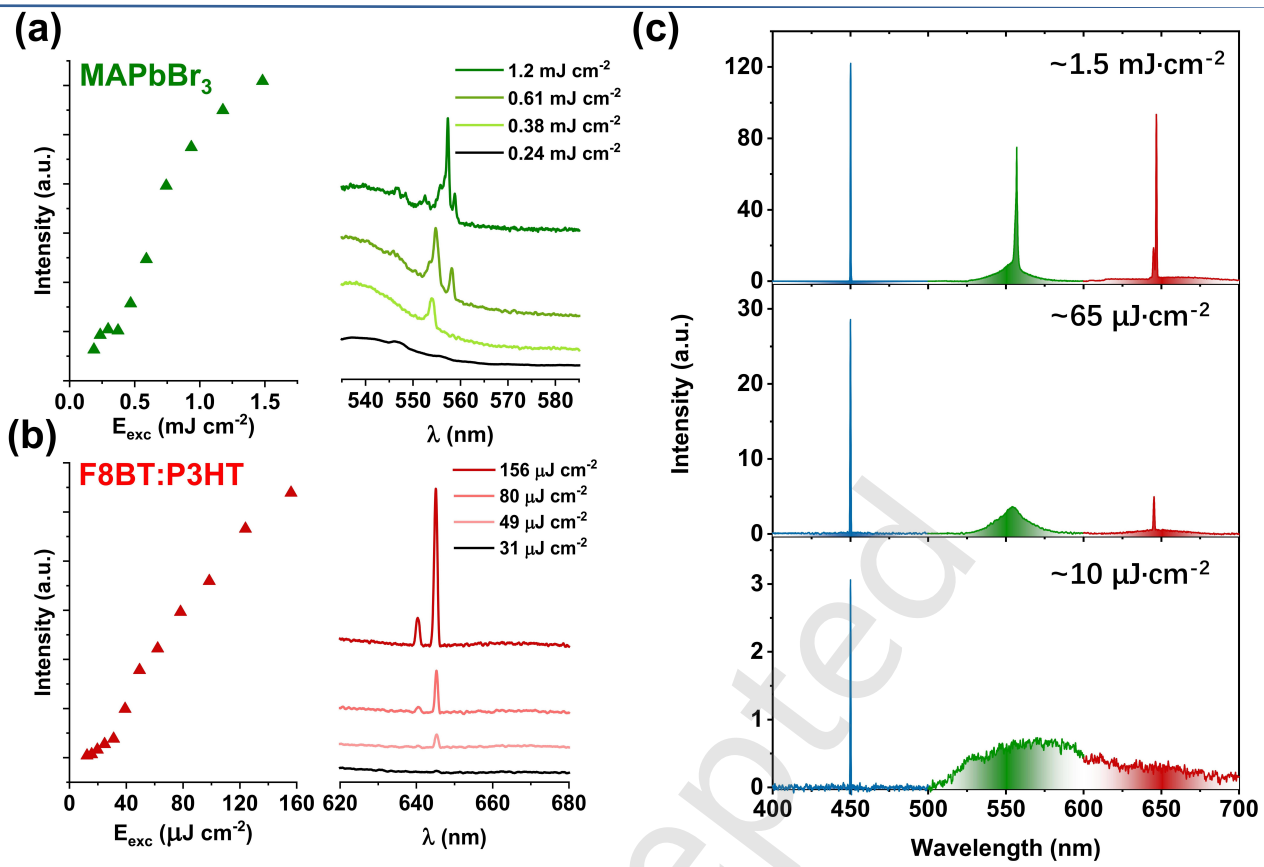


Figure 6 Output intensity (left) and the corresponding spectral evolution (right) as a function of excitation energy for the (a) $MAPbBr_3$ and (b) F8BT:P3HT layers of tandem device. (c) Full visible-spectrum (400–700 nm) coverage with a continuous baseline for the tandem device, acquired under various pumping energy densities.

role here. Nevertheless, the peak positions and FWHM valuesof the ASE spectra in the tandem and single-layer devices are comparable.

Following the ASE measurements, DFB lasers were developed under the same film preparation conditions. Two-dimensional (2D) second-order DFB gratings with periods of 330 nm and 390 nm were chosen as the resonator cavities for their superior light confinement over one-dimensional DFB gratings. The scanning electron microscope images of the DFB gratings are shown in Fig. S5 in the ESM. The two DFB gratings were fabricated on the same substrate and were positioned adjacent to one another. In keeping with the ASE measurements, the same 450 nm laser was used for excitation in the DFB laser tests. However, the beam was focused using a spheric lens rather than a cylindric one, producing a tiny circular spot on the samples instead of a stripe (see the "Experimental" section for details). From the ASE analysis and accompanying simulations, the film thicknesses of $MAPbBr_3$ and F8BT:P3HT in the tandem DFB laser device were adjusted to ~70 nm and ~130 nm, respectively. The single-layer DFB lasers, specifically, $MAPbBr_3$ (~70 nm thick) on 330 nm period gratings and F8BT:P3HT (~130 nm thick) on 390 nm period gratings were characterized first. The single-layer laser device performance is shown in Fig. S6 (ESM), while the results are summarized in Table 1, compared with those of the tandem DFB lasers. The thresholds of the $MAPbBr_3$ and F8BT:P3HT single-layer DFB lasers are 36 and 11 μJ cm^{-2}, with peak emission at 559 nm (linewidth 0.8 nm) and 653 nm (linewidth 0.6 nm), respectively. The tandem device was photoexcited from the polymer side, whereas the emitted light was collected from the substrate side. Therefore, reabsorption of the perovskite emission by the polymer blend can be largely avoided. To achieve simultaneous lasing from both media, the excitation laser spot was positioned at the junction of the two gratings with an enlarged beam size (see details in "Experimental" section). Figures 6(a) and 6(b) display the respective laser performances of $MAPbBr_3$ and F8BT:P3HT derived from the tandem DFB laser measurements. In Figs. 6(a) and 6(b), the left panels show the output density as a function of excitation fluence, while the right panels display the spectra measured at various excitation energies. The nonlinear output behavior reveals laser thresholds of 480 μJ·cm^{-2} for $MAPbBr_3$ and 43 μJ·cm^{-2} for F8BT:P3HT. Relative to their single-layer counterparts, the laser thresholds increased, following a trend similar to that observed in the ASE measurements. Owing to the re-absorption and the weakened light confinement introduced by the overlying F8BT:P3HT layer, the lasing threshold increase for $MAPbBr_3$ is more pronounced in the tandem device. Nonetheless, the threshold of 480 μJ·cm^{-2} is acceptable, especially given the ultra-compact thin-film device configuration. The spectra in the right panels show a clear trend toward ultranarrow laser lines, with peaks at ~557 nm for $MAPbBr_3$ and ~645 nm for F8BT:P3HT, and corresponding linewidths of 1.1 nm and 1.0 nm, respectively. The broader linewidths relative to those of the single-layer devices (see Table 1) may be attributed to the lower cavity Q-factor and reduced mode selectivity in the tandem device. The peak shift is ascribed to the effective index variation resulting from the layer stacking.

Figure 6(c) shows the continuous spectral coverage across the visible range (400–700 nm), recorded from the tandem device at various pump fluences. In all three panels, the blue excitation laser (450 nm) is present in the spectra with a linewidth of 0.6 nm. At a low pump fluence (~10 μJ cm^{-2}), only a broad PL

Just Accepted

band was observed, as shown in the bottom panel. As the fluence increased (~65 μJ cm^{-2}), red laser emission emerged first owing to the lower threshold (~43 μJ cm^{-2}) of the polymer blend (middle panel). When the pump fluence was further raised above the thresholds of both gain media in the tandem device (~1.5mJ cm^{-2}), dual-peak lasing at green and red wavelengths appeared (top panel). Since the tandem device was ultrathin, only a fraction of the pump light was absorbed by the films. The blue laser served not only as the excitation source but also as one of the three primary color sources in the device as shown in Fig. 6(c). Therefore, the RGB lasing in the organic/perovskite tandem device was demonstrated, which combined the blue excitation laser with the green and red emissions from the gain media. All parameters of the tandem DFB lasers are summarized in Table 1.

Table 1 Key parameters of the ASE and laser behavior measured in the single-layer and tandem devices.

	λ_{ASE} [a] [nm]	$E_{th\ ASE}$ [b] [μJ·cm^{-2}]	FWHM [nm]	λ_{laser} [c] [nm]	$E_{th\ laser}$ [d] [μJ·cm^{-2}]	FWHM [nm]
$MAPbBr_3$ Single-layer	549	73	4.4	559	36	0.8
$MAPbBr_3$ in $MAPbBr_3$/F8BT:P3HT	548	251	4.3	557	480	1.1
F8BT:P3HT Single-layer	656	6.8	12	653	11	0.6
F8BT:P3HT in $MAPbBr_3$/F8BT:P3HT	655	316	11	645	43	1

[a]ASE peak position; [b] ASE energy threshold; [c] laser peak position; [d] laser energy threshold.

3 Conclusion

The organic/perovskite tandem DFB laser was successfully fabricated via a simple spin coating method. Favorable gain property, solvent tolerance and optical confinement make perovskite an attractive partner for organic materials in tandem laser devices. Since both gain media in the tandem device can be effectively excited by a single 450 nm blue laser, this configuration holds promise for enabling indirectly electrically pumped lasers using commercial high-efficiency blue LEDs. Electromagnetic simulations were used to determine the device fabrication parameters. The ASE peak positions of $MAPbBr_3$ (~548 nm) and the F8BT:P3HT blend (~655 nm) in the tandem device show negligible shift relative to their single-layer references (~549 nm and ~656 nm, respectively), confirming good agreement between simulation and experiment results. Nevertheless, the increased ASE thresholds observed in the tandem device, rising from 73 to 251 μJ·cm^{-2} for $MAPbBr_3$ and from 6.8 to 316 μJ·cm^{-2} for the F8BT:P3HT blend, necessitate further optimization, such as better optical mode matching or refined device architecture, to compensate for the introduced losses. Further, by sequentially depositing the perovskite and polymer blend onto a substrate pre-patterned with two adjacent 2D DFB gratings (periods: 330 nm and 390 nm), dual-wavelength lasing at 557 nm and 645 nm was achieved in a single tandem device under 450 nm laser excitation. RGB lasing was realized in a single device when the pump fluence exceeded the ~480 μJ·cm^{-2} threshold. The transmitted blue pump laser naturally served as the blue spectral component. In future development, well-designed DFB grating arrays can be integrated onto the substrate to function as individual pixels in high-resolution RGB laser display panels. Furthermore, the blue excitation laser used in this work could potentially be replaced by electrically driven LEDs, enabling indirectly electrically pumping. This concept thus paves the way for ultra-compact, full-visible-band nanolasers for next-generation display technologies.

4 Experimental

Materials and thin films preparation: F8BT (Mw:10000-100000), P3HT (Mw:10000-100000), methylammonium bromide (MABr, 99.5%) and lead acetate ($Pb(OAc)_2$, 99.5%) were purchased from Xi'an Polymer Light Technology Corp. N,N-dimethylformamide (DMF, GC, 99.9%) was purchased from Shanghai Macklin Biochemical Co.,Ltd. Toluene (GC, 99.5%) was purchased from Nanjing Chemical Reagent Co., LTD. All the materials and solvents were used as received without further purification.

The quartz substrates (12 mm × 12 mm) and DFB gratings (on silica wafer) used in this study were sequentially cleaned by detergent, deionized water, acetone, and anhydrous ethanol in an ultrasonic bath for 15 min of each step. Subsequently, the substrates and DFB gratings were plasma-cleaned for 4 min before the spin-coating process.

The perovskite ($MAPbBr_3$) precursor solution was prepared by mixing MABr and $Pb(OAc)_2$ at a 3:1 molar ratio in DMF with different concentrations (namely, $Pb(OAc)_2$ 0.2, 0.4, 0.5, 0.6, 0.8, and 1.0 M), under magnetic stirring for 8 hours. Then the solution was spin-coated onto the quartz substrate or DFB grating at a speed of 6000 rpm for 30 s in a nitrogen filled glovebox. Then, the film was annealed at 100 ℃ for 5 min.

F8BT:P3HT (85:15 wt.%, 25 mg·mL^{-1} in toluene) blend solution was prepared in the same glovebox. The solution was heated and stirred overnight to ensure completely dissolving of polymers. The film was spin-coated onto the perovskite layer immediately after the perovskite annealing process, at a speed of 4000 rpm.

Absorption and Photoluminescence (PL) measurements: The Lambda 35 UV-vis spectrophotometer from PerkinElmer with a deuterium lamp providing 200-400 nm and a tungsten lamp providing 400-900 nm radiation sources, respectively, was used

Just Accepted

for absorption measurements. The fluorescence spectrophotometer RF-6000 from SHIMADZU was used for PL measurements. All film samples used in these measurements are same to those used in ASE measurements.

Film thickness measurements: The instrument used was the DektakXT Stylus step (Bruker Co.). Standard scan mode was used.

AFM measurements: Surface topography of the thin films was characterized using a Dimension Icon atomic force microscope (Bruker Co.). "Tapping mode" was used in all measurements. The surface roughness was determined by numerical fitting of the acquired profiles.

ASE measurements: In ASE measurements, film samples (slab waveguides) were optically pumped at selected wavelength (450 nm) with a type-II β-BaB_2O_4 [BBO] optical parametric oscillator (Panther EX) pumped by a Q-switched, neodymium ion doped yttrium aluminum garnet (Nd^{3+}:YAG) laser (Continuum Surelite II-10). The laser delivered 5 ns pulses at a 10 Hz repetition rate. The excitation laser passed through an adjustable slit and a cylindrical lens (focal length=10 cm), in sequence, forming a 550 μm × 4 mm stripe. The excitation laser was attenuated using a set of calibrated neutral density filters placed in the beam path. Output signals were collected at the sample edge by a fiber coupled grating spectrometer (SR-500i-D2, Andor Co.) equipped with a CCD detector (DU940P-UV, Newton Co.). The energy of the excitation pulse was determined with an energy/power meter. (LabMax-TOP, Coherent Co.) Strictly, there is no a univocal way to describe ASE threshold ($E_{th\ ASE}$). We defined the $E_{th\ ASE}$ values as the incident pulse energy when the FWHM of the recorded spectra falls to half of the initial value measured in PL spectrum. At low excitation fluences, the PL intensity scales linearly with fluence and exhibits no observable linewidth narrowing, until a threshold fluence is exceeded. Beyond this point, spontaneously emitted photons that are waveguided along the irradiated stripe-shaped gain region undergo amplification via stimulated emission, and are eventually emitted from the ends of the stripe. Therefore, the spectra become narrow with a significant increase in the output peak intensity.

DFB laser measurements: The DFB lasers were optically pumped with the same source and detected using the same equipment as described above in ASE measurements. DFB lasers were fabricated by spin coating active mediums on top of the pre-patterned silica substrates with 2D surface grating (Λ=330 nm and 390 nm, depth=70 nm and fill factor=50%). The two DFB gratings were fabricated on the same substrate and were positioned adjacent to one another. The pumping laser beam was focused by a spherical lens (focal length =10 cm). The output laser beam was collected in the direction normal to the substrate. The excitation area was a circular spot with 280 μm in diameter (6.15 x 10^{-4} cm^2 in area). In tandem device measurements, the excitation laser spot was positioned at the junction of the two gratings with an enlarged beam size (1.96 x 10^{-3} cm^2 in area, achieved by slightly defocusing the spherical lens). The "Step and Glue" function was utilized in the acquisition setup to acquire spectra spanning the entire visible region (400-700 nm). For single-layer and tandem devices, the pump light was always incident from the film side, whereas the emission was collected from the substrate side.

Optical waveguide simulation: In order to simulate the optical modes of single-layer and tandem devices, the COMSOL Multiphysics software was employed. The waveguide model was two-dimensional (X-Y) and was constructed based on the multilayer structure. The refractive indices (n) were measured experimentally as shown in the ESM. Here, we consider only the transverse electric (TE) mode, which was calculated by solving the following frequency-domain wave equation.

$$\nabla\times(\nabla\times\boldsymbol{E})-k_0^2\varepsilon_r\boldsymbol{E}=0 \quad (1)$$

where ε_r (relative permittivity) was computed from $\varepsilon_r=(n-ik)^2$. In order to solve this equation, we applied 'scattering-type' boundary conditions at the top air interface and the bottom quartz layer. A 'perfect' electrical conductor boundary condition was used on the left and right sides of the model, and one boundary of the waveguide structure was set to a 'user-defined' port, and the polarization of the electrical mode field from the excitation source was set to the Z-direction. Then, the mode confinement factor of each calculated layer (Γcalc) was calculated from:

$$\Gamma calc=\frac{\int_{calc}|E|^2dx\,dy}{\int_{-\infty}^{+\infty}|E|^2dx\,dy} \quad (2)$$

Electronic Supplementary Material: Supplementary material (please provide the brief detail of the ESM) is available in the online version of this article at https://doi.org/10.26599/NR.2026.94909212.

Data availability

All data needed to support the conclusions in the paper are presented in the manuscript and/or the Electronic Supplementary Material. Additional data related to this paper may be requested from the corresponding author upon request.

Acknowledgements

We thank the National Natural Science Foundation of China (Grants 61874058). Qi Zhang thanks the financial support from National Natural Science Foundation of China (Grant No. 62405143), Natural Science Foundation of Jiangsu Province (Grant No. BK20240639), the Natural Science Foundation of the Jiangsu Higher Education Institutions of China (Grant No. 23KJB510018) and the Natural Science Research Start-up Foundation of Recruiting Talents of Nanjing University of Posts and Telecommunications (Grant No. NY223151). Junbiao Peng thanks the financial support from National Natural Science Foundation of China (Grant No.22090024) and Songshan Lake Materials Laboratory (20221633).

Declaration of competing interest

The other contributing authors report no conflict of interests in this work.

Author contribution statement

Ruidong Xia conceived the idea of the organic/perovskite tandem RGB DFB nanolasers, supervised the research project and oversaw the manuscript preparation. Qi Zhang fabricated the DFB cavities, performed DFB lasers tests and data analysis, and wrote the manuscript. Zhiyuan Zhang, Xuanxuan Wei, and Zihan Xiao fabricated the ASE devices, performed the tests and simulation of waveguiding modes in multilayer device. Junbiao Peng contributed to data processing and manuscript preparation.

Just Accepted

Informed consent
Not applicable.

Ethics statement
Not applicable.

Use of AI statement
None.

References

[1] Fuchsberger, J.; Letsou, T. P.;Kazakov, D.; Szedlak, R.;Capasso, F.; Schwarz, B. Continuously and widely tunable semiconductor ring lasers. *Optica* **2025**, *12*, 985-990.

[2] Szukalska, A. Quantum Dot-Driven Innovations in Multicolor Lasing and Laser Display Applications. *Laser Photonics Rev.* **2026** *20*, e02430.

[3] Zhuang, X.; Ouyang, Y.; Wang, X.; Pan, A. Multicolor Semiconductor Lasers. *Adv. Opt. Mater.* **2019**, *7*, 1900071.

[4] Burghart, D.; Zhang, K.; Oberhausen, W.; Köninger, A.;Boehm, G.; Belkin, M. A. Multi-color photonic integrated circuits based on homogeneous integration of quantum cascade lasers. *Nat. Commun.* **2025**, *16*, 3563.

[5] Li, X.; Du, J.; Jia, Y.; Hu, S.; Li, G.; Zhang, B.; Zhu, J.; Guo, J.; Wu, K. Stable, Efficient, and Scalable Multicolor Lasing from Colloidal Quantum Dots in Liquids. *ACS Nano* **2025**, *19*, 27488-27499.

[6] Song, X.; Xu, Z.; Gao, B.; Li, X.; Lv, Q.; Zhang, R.; Wang, B.; Zhang, H.; Guo, P.; Ho, J. C. Red–Green–Blue Light Emission from Composition Tunable Semiconductor Micro-Tripods. *Adv. Funct. Mater.* **2024**, *34*, 2403135.

[7] Yoshida, K.; Gong, J.; Kanibolotsky, A. L.; Skabara, P. J.; Turnbull, G. A.; Samuel, I. D. W. Electrically driven organic laser using integrated OLED pumping. *Nature* **2023**, *621*, 746-752.

[8] Ou, Q.; Peng, Q.; Shuai, Z. Computational screen-out strategy for electrically pumped organic laser materials. *Nat. Commun.* **2020**, *11*, 4485.

[9] Sandanayaka, A. S. D.; Matsushima, T.; Bencheikh, F.; Terakawa, S.; Potscavage, W. J.; Qin, C.; Fujihara, T.; Goushi, K.; Ribierre, J.-C.; Adachi, C. Indication of current-injection lasing from an organic semiconductor. *Appl. Phys. Express* **2019**, *12*, 061010.

[10] Zou, C.; Ren, Z.; Hui, K.; Wang, Z.; Fan, Y.; Yang, Y.; Yuan, B.; Zhao, B.; Di, D. Electrically driven lasing from a dual-cavity perovskite device. *Nature* **2025**, *645*, 369-374.

[11] Elkhouly, K.; Goldberg, I.; Zhang, X.; Annavarapu, N.; Hamdad, S.; Croes, G.; Rolin, C.; Genoe, J.; Qiu, W.; Gehlhaar, R.; Heremans, P. Electrically assisted amplified spontaneous emission in perovskite light-emitting diodes. *Nat. Photon.* **2024**, *18*, 132-138.

[12] Yang, B.; Liu, M.; Xu, T.; Wei, Y.; Sha, S.; Wan, P.; Kan, C.; Shi, D.; Jiang, M. Surface modification of metal nanostructures toward electrically pumped perovskite microlasers. *Sci. China Mater.* **2025**, *69*, 149–160.

[13] Grede, A. J.; Cawthorn, R.; Zhao, L.; Murphy, J. P.; Roh, K.; Al Kurdi, K.; Barlow, S.; Marder, S. R.; Rand, B. P.; Giebink, N. C. Electrically Assisted Lasing in Metal Halide Perovskite Semiconductors. *ACS Photonics* **2024**, *11*, 1851-1856.

[14] Shi, Y.; Deng, X.; Gan, Y.; Xu, L.; Zhang, Q.; Xiong, Q. Ten Years of Perovskite Lasers. *Adv. Mater.* **2025**, *37*, 2413559.

[15] Ke, Y.; Zhu, W.; Ma, C.; Xiong, K.; Liu, W.; Kuang, Z.; Wu, J.; Qian, D.; Li, M.; Wang, S.; Wang, J.; Tao, X.; Xu, S.; Zhu, L.; Peng, Q.; Wang, N.; Huang, W.; Wang, J. High-performance tandem perovskite LEDs through interlayer photon recycling. *Nature* **2026**, *649*, 53-58.

[16] Zhang, H.; Su, Q.; Chen, S. Quantum-dot and organic hybrid tandem light-emitting diodes with multi-functionality of full-color-tunability and white-light-emission. *Nat. Commun.* **2020**, *11*, 2826.

[17] Jia, Z.; Guo, X.; Yin, X.; Sun, M.; Qiao, J.; Jiang, X.; Wang, X.; Wang, Y.; Dong, Z.; Shi, Z.; Kuan, C.-H.; Hu, J.; Zhou, Q.; Jia, X.; Chen, J.; Wei, Z.; Liu, S.; Liang, H.; Li, N.; Lee, L. K.; Guo, R.; Roth, S. V.; Müller-Buschbaum, P.; Hao, X.; Du, X.; Hou, Y. Efficient near-infrared harvesting in perovskite–organic tandem solar cells. *Nature* **2025**, *643*, 104-110.

[18] Sun, S.-Q.; Cai, Y.; Zhu, M.; He, W.; Liu, B.-C.; Xu, Y.-L.; Lv, X.; Sun, Q.; Liu, P.; Shi, T.; Xie, Y.-M.; Fung, M.-K. Highly Efficient Hybrid Perovskite/Organic Tandem White Light Emitting-Diodes with External Quantum Efficiency Exceeding 20%. *Adv. Funct. Mater.* **2023**, *33*, 2306549.

[19] Brinkmann, K. O.; Wang, P.; Lang, F.; Li, W.; Guo, X.; Zimmermann, F.; Olthof, S.; Neher, D.; Hou, Y.; Stolterfoht, M.; Wang, T.; Djurišić, A. B.; Riedl, T. Perovskite–organic tandem solar cells. *Nat. Rev. Mater.* **2024**, *9*, 202-217.

[20] Kong, L.; Luo, Y.; Wu, Q.; Xiao, X.; Wang, Y.; Chen, G.; Zhang, J.; Wang, K.; Choy, W. C. H.; Zhao, Y.-B.; Li, H.; Chiba, T.; Kido, J.; Yang, X. Efficient and stable hybrid perovskite-organic light-emitting diodes with external quantum efficiency exceeding 40 per cent. *Light Sci. Appl.* **2024**, *13*, 138.

[21] An, Y.; Zhang, N.; Liu, Q.; Jiang, W.; Du, G.; Chen, D.; Liu, M.; Huang, X.; Lei, T.; Qiu, Q.; Lin, F. R.; Zeng, X. C.; Jen, A. K. Y.; Yip, H.-L. Balancing carrier transport in interconnection layer for efficient perovskite/organic tandem solar cells. *Nat. Commun.* **2025**, *16*, 2759.

[22] Nie, L.; Wang, T.; Yu, X.; Gao, W.; Peng, Q.; Xia, Z.; Qiu, J.; Yu, S. F.; Xu, X. Multicolor Display Fabricated via Stacking CW Laser-Patterned Perovskite Films. *ACS Energy Lett.* **2023**, *8*, 2025-2032.

[23] Zhang, Q.; Li, J.; Yu, Z.; Xiang, P.; Xiao, L.; Lei, J. Laser-Induced Fabrication of Multicolor Perovskite Quantum Dot Patterns with Multiple Information Encryption Modes. *ACS Appl. Mater. Interfaces* **2025**, *17*, 14350-14359.

[24] Liang, J.; Chu, M.; Zhou, Z.; Yan, Y.; Zhao, Y. S. Optically Pumped Lasing in Microscale Light-Emitting Electrochemical Cell Arrays for Multicolor Displays. *Nano Lett.* **2020**, *20*, 7116-7122.

[25] Zhang, Q.; Sun, H.; Zhang, H.; Jiang, M.; Wu, X.; Zhang, Z.; Yang, T.; Xia, R.; Cabanillas-Gonzalez, J. Facile and Controllable Fabrication of High-Performance Methylammonium Lead Triiodide Films Using Lead Acetate Precursor for Low-Threshold Amplified Spontaneous Emission and Distributed-Feedback Lasers. *Phys. Status Solidi RRL* **2019**, *13,* 1900176.

[26] Zhang, Z.; Zhang, Q.; Wei, X.; Xiao, Z.; Zhu, S.; Fu, S.; Sun, H.; Florica, C.; Peng, J.; Xia, R. Dual-Color Lasers in Interlayer-Free Solution Processed Polymeric Bilayer Devices. *ACS Appl. Mater. Interfaces* **2023**, *15*, 39797-39806.

[27] Smirnov, J. R. C.; Sousaraei, A.; Osorio, M. R.; Casado, S.; Hernández, J. J.; Wu, L.; Zhang, Q.; Xia, R.; Granados, D.; Wannemacher, R.; Rodriguez, I.; Cabanillas-Gonzalez, J. Flexible distributed feedback lasers based on nanoimprinted cellulose diacetate with efficient multiple wavelength lasing. *npj Flex. Electron.* **2019**, *3*, 17.

[28] Wu, L.; Luo, F.; Lüer, L.; Romero, B.; Manuel Otón, J.; Zhang, Q.; Xia, R.; Cabanillas-Gonzalez, J. Quantifying the efficiency of förster-assisted optical gain in semiconducting polymer blends by excitation wavelength selective amplified spontaneous emission. *J. Polym. Sci. Part B: Polym. Phys.* **2016**, *54*, 2311-2317.

[29] Xia, R.; Stavrinou, P. N.;Bradley, D. D. C.; Kim, Y. Efficient optical gain media comprising binary blends of poly(3-hexylthiophene) and poly(9,9-dioctylfluorene-co-benzothiadiazole). *J. Appl. Phys.* **2012**, *111*, 123107.

[30] Wu, L.; Casado, S.; Romero, B.; Otón, J. M.; Morgado, J.; Müller, C.; Xia, R.; Cabanillas-Gonzalez, J. Ground State Host-Guest Interactions upon Effective Dispersion of Regioregular Poly(3-hexylthiophene) in Poly(9,9-dioctylfluorene-alt-benzothiadiazole). *Macromolecules* **2015**, *48*, 8765–8772.

[31] Wu, L.; Nieto-Ortega, B.; Naranjo, T.; Pérez, E. M.; Cabanillas-Gonzalez J. Entropy-Driven Heterocomplexation of Conjugated Polymers in Highly Diluted Solutions. The *J. Phys. Chem. C* **2019**, *123*,16596–16601.

Just Accepted

Electronic Supplementary Material

Tandem organic–perovskite heterostructures toward red/green/blue distributed feedback lasers

Qi Zhang[1,2], Zhiyuan Zhang[2,3], Xuanxuan Wei[2], Zihan Xiao[2], Junbiao Peng[3] and Ruidong Xia[2]

1 School of Electronic and Optical Engineering, School of Flexible Electronics (Future Technology), Nanjing University of Posts and Telecommunications, Nanjing 210023, China
2 Key Laboratory for Organic Electronics & Information Displays (KLOEID), Jiangsu-Singapore Joint Research Center for Organic/Bio Electronics & Information Displays, Institute of Advanced Materials (IAM), Nanjing University of Posts and Telecommunications, 9 Wenyuan Road, Nanjing 210046, China
3 National Key Laboratory of Luminescence Materials and Devices, South China University of Technology, Guangzhou 510641, China

Address correspondence to Ruidong Xia, iamrdxia@njupt.edu.cn; Junbiao Peng, psjbpeng@scut.edu.cn

Supporting information to https://doi.org/10.26599/NR.2026.94909212

Just Accepted

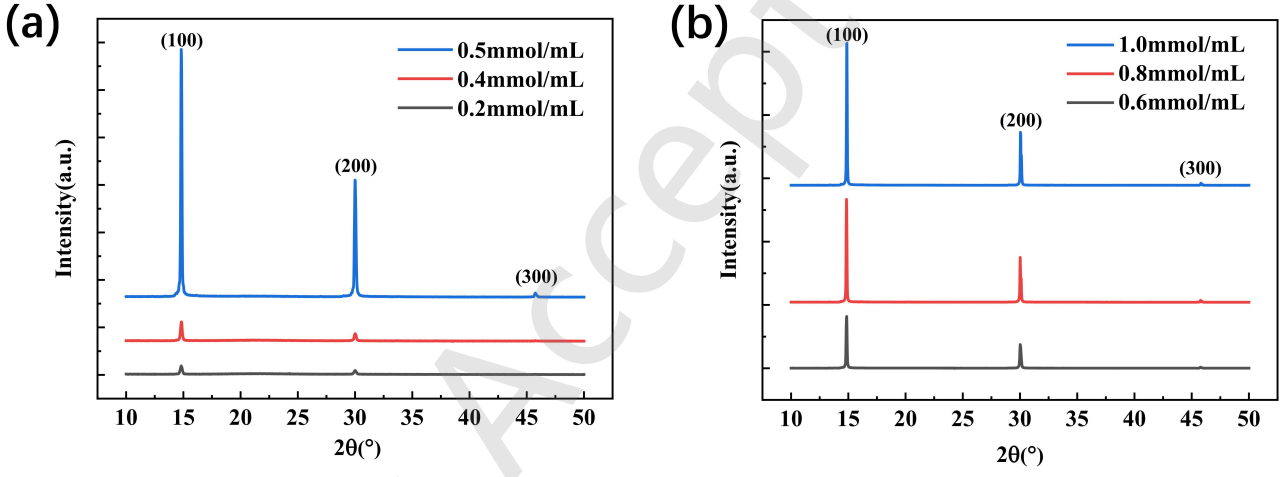


Figure S1 X-ray diffraction (XRD) spectra of $MAPbBr_3$ film fabricated from precursor solutions with varied lead acetate concentrations: (a) 0.2, 0.4, 0.5 and (b) 0.6, 0.8 1.0 mmol/mL). For all samples, the characteristic diffraction peaks at 14.82°, 30.02° and 45.75° corresponding to the (100), (200) and (300) crystal planes of the perovskite cubic phase are clearly observed.

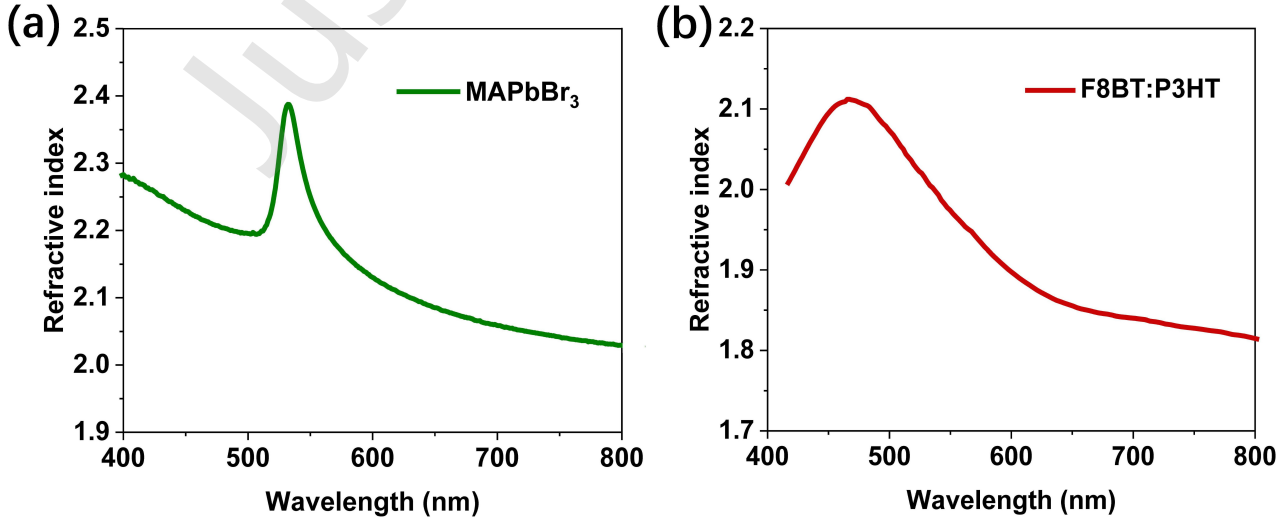


Figure S2 Refractive index of (a) $MAPbBr_3$ and (b) F8BT:P3HT blend films.

Address correspondence to First A. Firstauthor, email1; Third C. Thirdauthor, email2

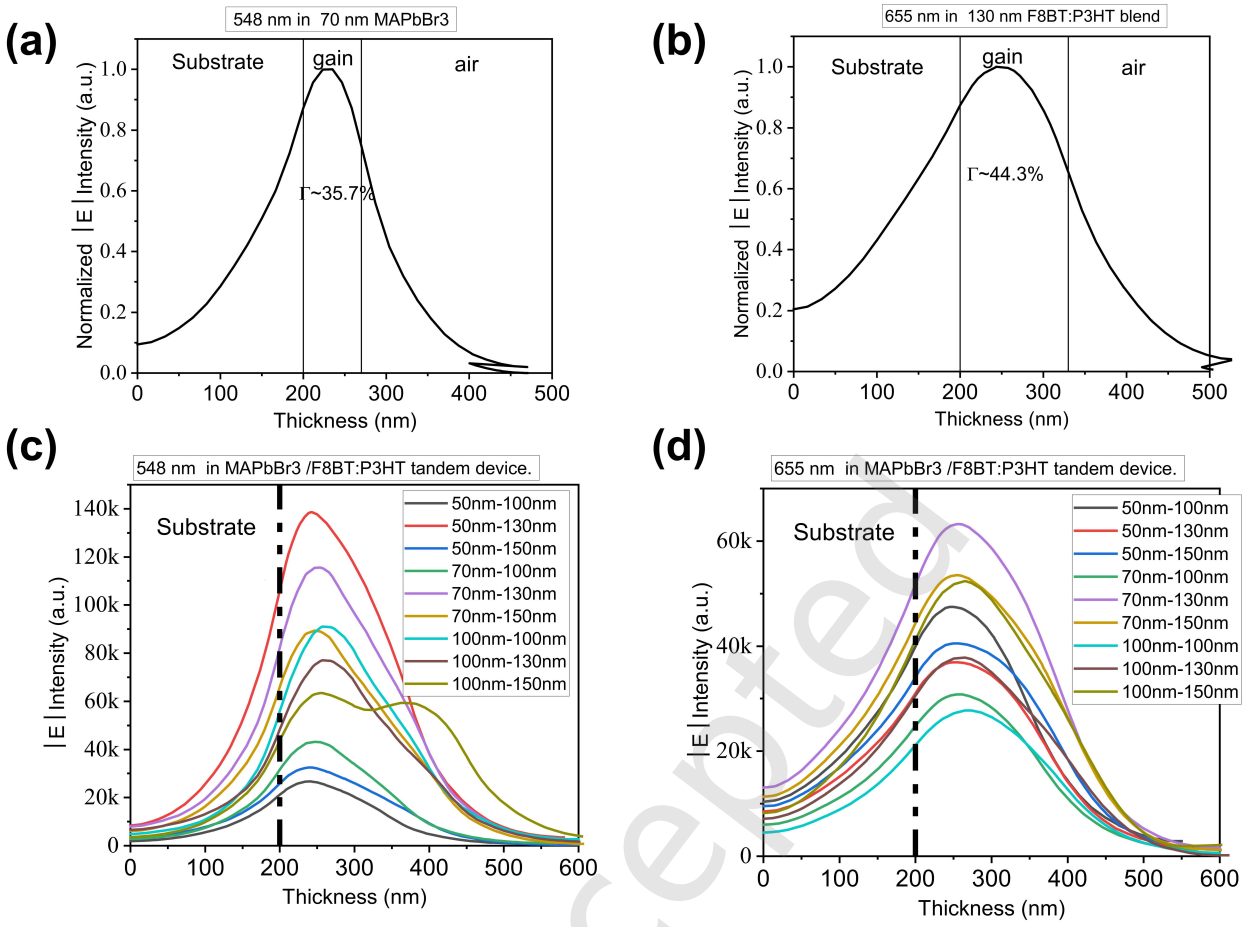


Figure S3 Distribution of the transverse electric field profiles (normalized) for characteristic modes in single-layer and tandem devices: (a) at 548 nm in a $MAPbBr_3$ single-layer device (70 nm thick); (b) at 655 nm in an F8BT:P3HT blend single-layer device (130 nm thick); (c) at 548 nm and (d) at 655 nm in tandem devices consisting of F8BT:P3HT and $MAPbBr_3$ under non-optimized conditions. Γ denotes the confinement factor in the active layer.

Just Accepted

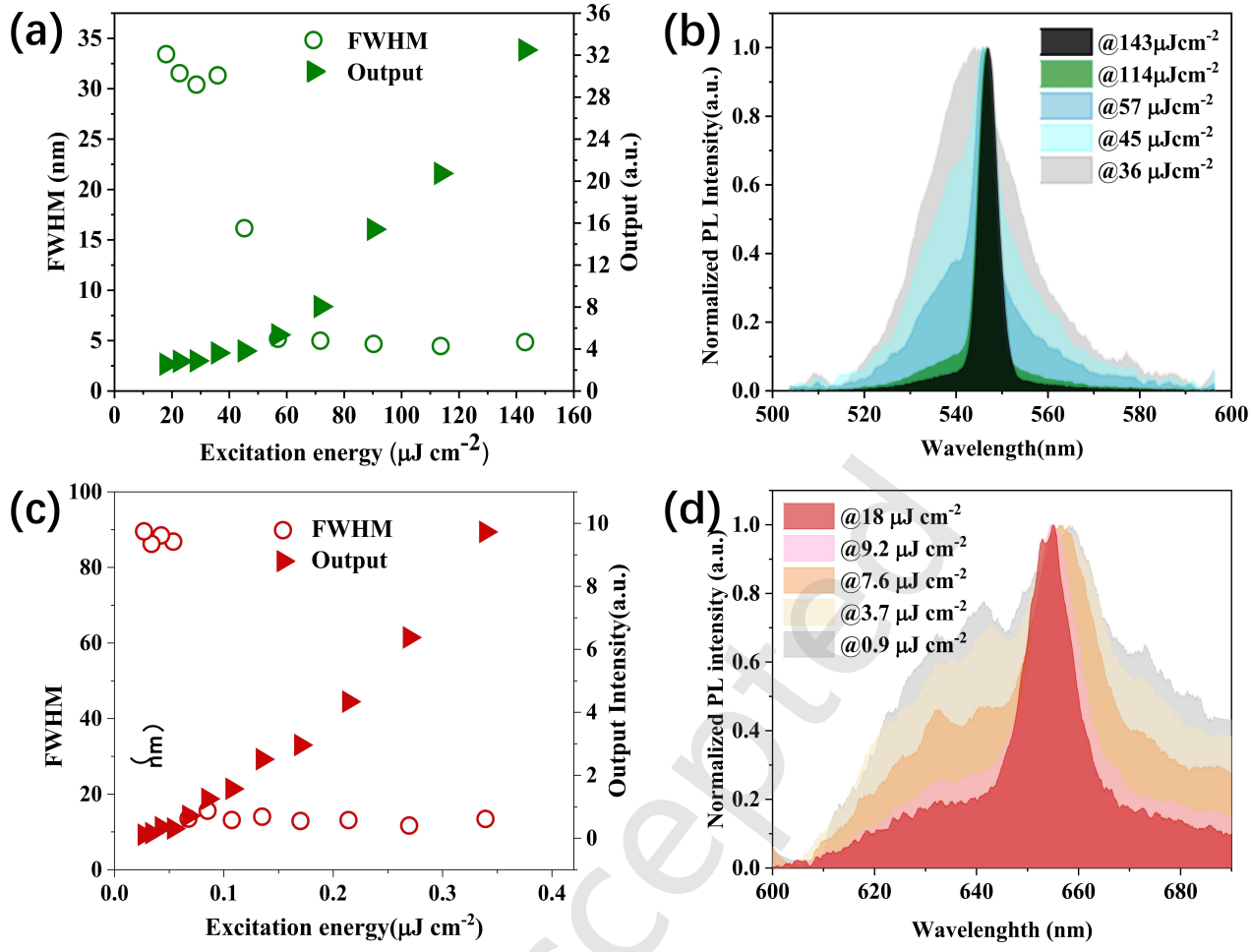


Figure S4 Output intensity and FWHM versus excitation energy, along with the corresponding spectral evolution measured for the $MAPbBr_3$ ((a) and(b)) and F8BT:P3HT ((c) and (d)) single-layer devices.

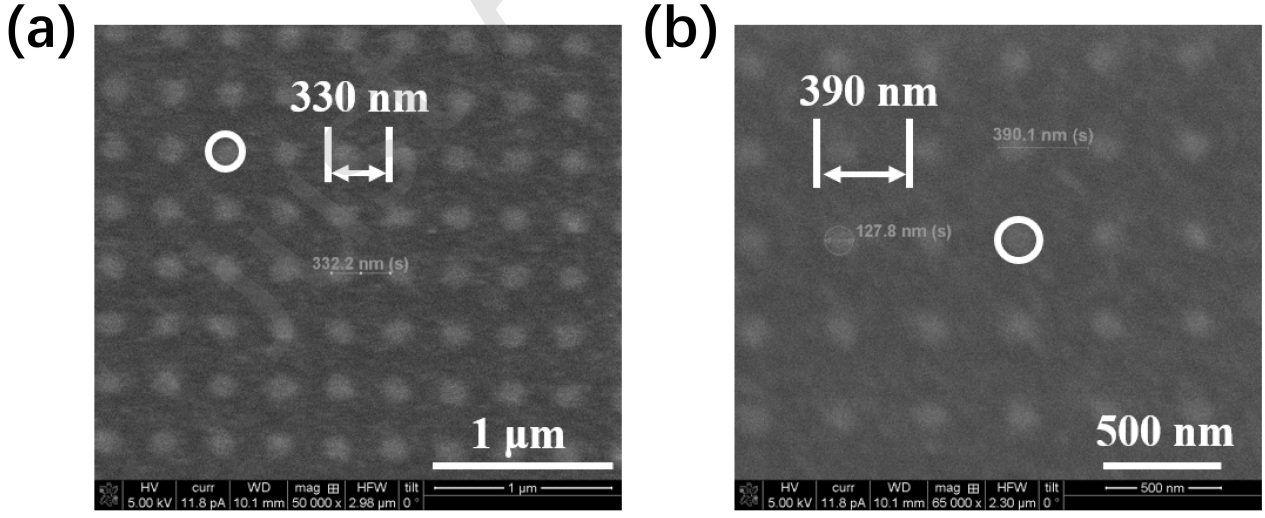


Figure S5 Scanning electron images (SEM) images of the DFB cavities with periods of 330 nm (a) and 390 nm (b) used in this work.

Accepted

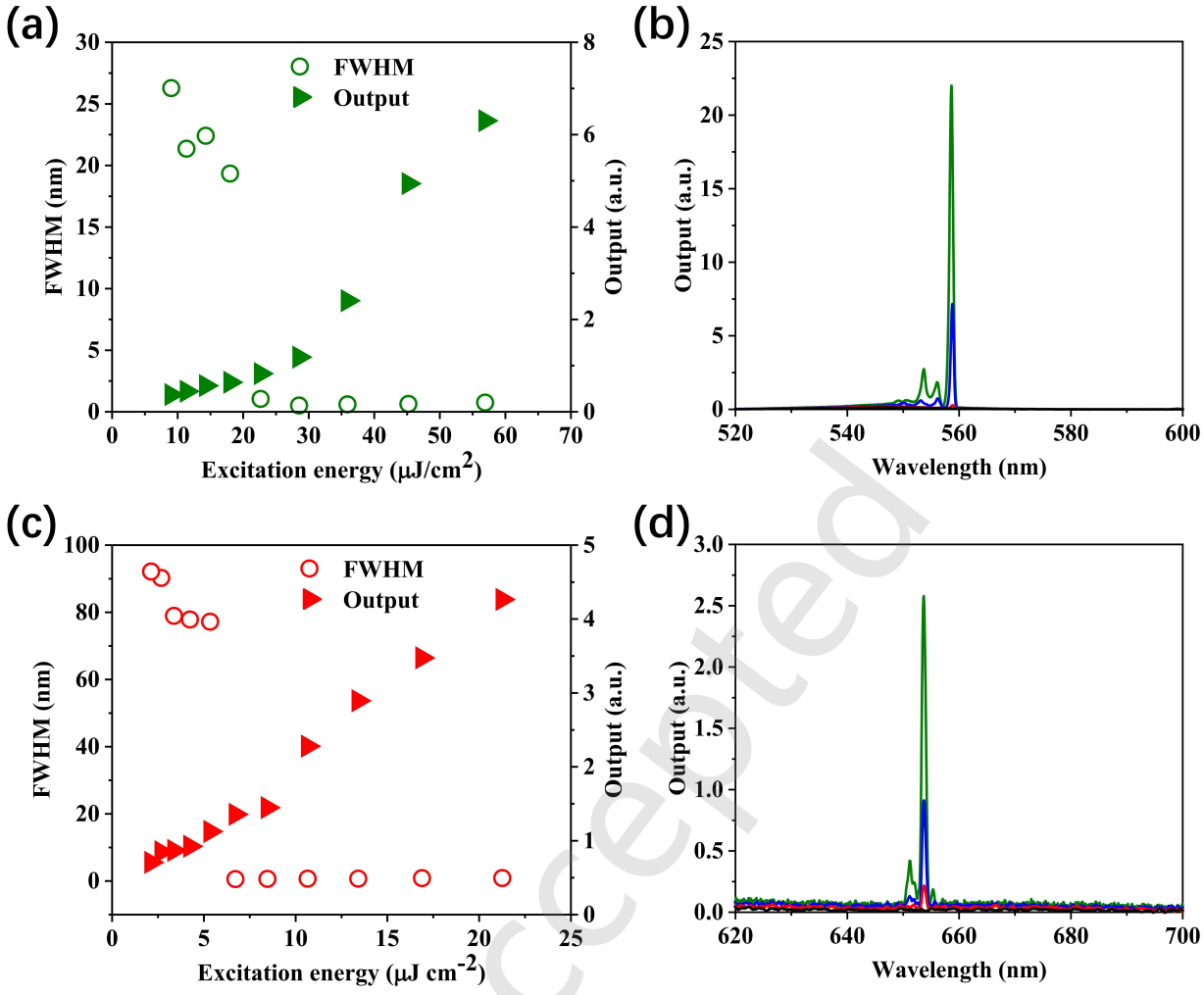


Figure S6 Output intensity and FWHM versus excitation energy, along with the corresponding laser spectra, measured for the $MAPbBr_3$ DFB laser (with a 330 nm period cavity, (a) and(b)) and F8BT:P3HT DFB laser (with a 390 nm period cavity, (c) and (d)).

Just Accepted